Prospects for measurements of the longitudinal proton structure function F_L at the Electron Ion Collider

Javier Jiménez-López*

Universidad de Alcalá, Departamento de Física y Matemáticas, Facultad de Ciencias, 28805 Alcalá de Henares, Madrid, Spain

Paul R. Newman

School of Physics and Astronomy, University of Birmingham, Birmingham B15 2TT, United Kingdom

Katarzyna Wichmann

Deutsches Elektronen-Synchrotron DESY, Germany

(Received 17 January 2025; accepted 10 February 2025; published 13 March 2025)

We explore the potential for extracting the longitudinal proton structure function F_L at the future Electron Ion Collider (EIC) through a Rosenbluth separation method. The impacts of differing assumptions on sample sizes, systematic uncertainties, and beam energy scenarios are investigated. With a sufficiently large number of center-of-mass energy configurations and well-controlled systematics, the EIC will measure F_L to an unprecedented precision, even with relatively modest luminosities. The accessible kinematic range complements both fixed-target and Hadron-Electron Ring Accelerator data. In the most optimistic scenarios, the EIC data will be a highly competitive direct probe of the proton gluon density.

DOI: 10.1103/PhysRevD.111.056014

I. INTRODUCTION

The investigation of the internal structure of the proton is an important topic in high-energy physics, offering deep insights into the composition and dynamics of strongly interacting matter. Central to these studies has been the measurement of cross sections for deep inelastic scattering (DIS) and thus of the proton structure functions, which in turn provide insight into the distributions of quarks and gluons in the nucleon [1]. The Hadron-Electron Ring Accelerator (HERA) was the first and to date the only electron-proton colliding beam facility. It allowed measurements of inclusive DIS cross sections, and extraction of the structure functions F_2, F_L, and $xF_3^{\gamma Z}$ [2]. Among these, the longitudinal structure function F_L plays a special role through its direct, approximately linear, dependence on the gluon density, which has been widely exploited in fits for proton parton densities [3–6] and phenomenological models [7–9]. Knowledge of both the F_2 and F_L structure functions equivalently enables extractions of the ratio R between the inclusive cross sections for longitudinally to transversely polarized virtual photons to interact with the proton, according to $R = F_L/(F_2 - F_L)$.

The extractions of F_L at HERA [10,11] are limited by statistics and cover a restricted range in the Bjorken variable x and the squared four-momentum transfer Q^2. It has also been possible to obtain F_L for the proton at low Q^2 from numerous fixed-target DIS experiments [12–18]. The Electron-Ion Collider [19] (EIC), which is expected to begin science operations at Brookhaven National Laboratory in the early 2030s, promises to revolutionize our understanding of the internal structure of hadrons. With its capability to operate at high luminosities and to cover a wide range of beam energy configurations, the EIC will provide information in regions of x and Q^2 that are not well covered by previous experiments and are well suited to F_L extractions. In this study, we assess the EIC F_L capabilities by analyzing simulated "pseudodata" with varying assumptions on systematic precision and beam energy configurations.

II. EIC PSEUDODATA

The accelerator and detector designs for the EIC are currently undergoing intense development, but the overall specifications in terms of beam energy ranges and instrumentation coverage and performance are already well established [20]. The studies presented in this paper are based on simulated data points, or "pseudodata," which are derived from that baseline configuration. Our approach to

*Contact author: javier.jimenezl@edu.uah.es

TABLE I. Beam energies, center-of-mass energies, and integrated luminosities assumed for the different EIC configurations considered.

e-beam energy (GeV)	p-beam energy (GeV)	$\sqrt{s}$ (GeV)	Integrated lumi (fb^{-1})
18	275	141	15.4
10	275	105	100
10	100	63	79.0
5	100	45	61.0
5	41	29	4.4

producing inclusive DIS EIC pseudodata follows that of [21], which in turn took binning schemes based on those in the ATHENA detector proposal [22]. ATHENA collaboration has since merged with ECCE [23] to create ePIC collaboration, which is now rapidly converging toward a design for a first EIC detector. While some specifics of the detectors have evolved, the overall expected kinematic range, kinematic variable resolutions, and achievable experimental precision are largely independent of the detailed detector design, and this study is thus applicable to any general purpose EIC experiment.

As summarized in Table I, pseudodata are produced with integrated luminosities corresponding to expectations for one year of data collection in each of the five expected beam configurations at the EIC [20], giving five different center-of-mass energies $\sqrt{s}$. For each beam configuration, pseudodata are produced at five logarithmically spaced x values per decade over the inelasticity range $0.005 < y < 0.96$, matching the expected experimental resolutions [22]. The EIC resolution in Q^2 is expected to be significantly better than that of the HERA experiments, so for ease of comparison, we adopt the Q^2 values from the measurements of F_L in [10,11]. The central values of the pseudodata cross sections are initiated using Next-to-Next-to Leading Order (NNLO) theoretical predictions based on the HERAPDF2.0 parton densities [2] within the xFitter framework [24–26], with the Q^2 evolution performed according to the NNLO DGLAP evolution equations [27–36]. The value for each data point is

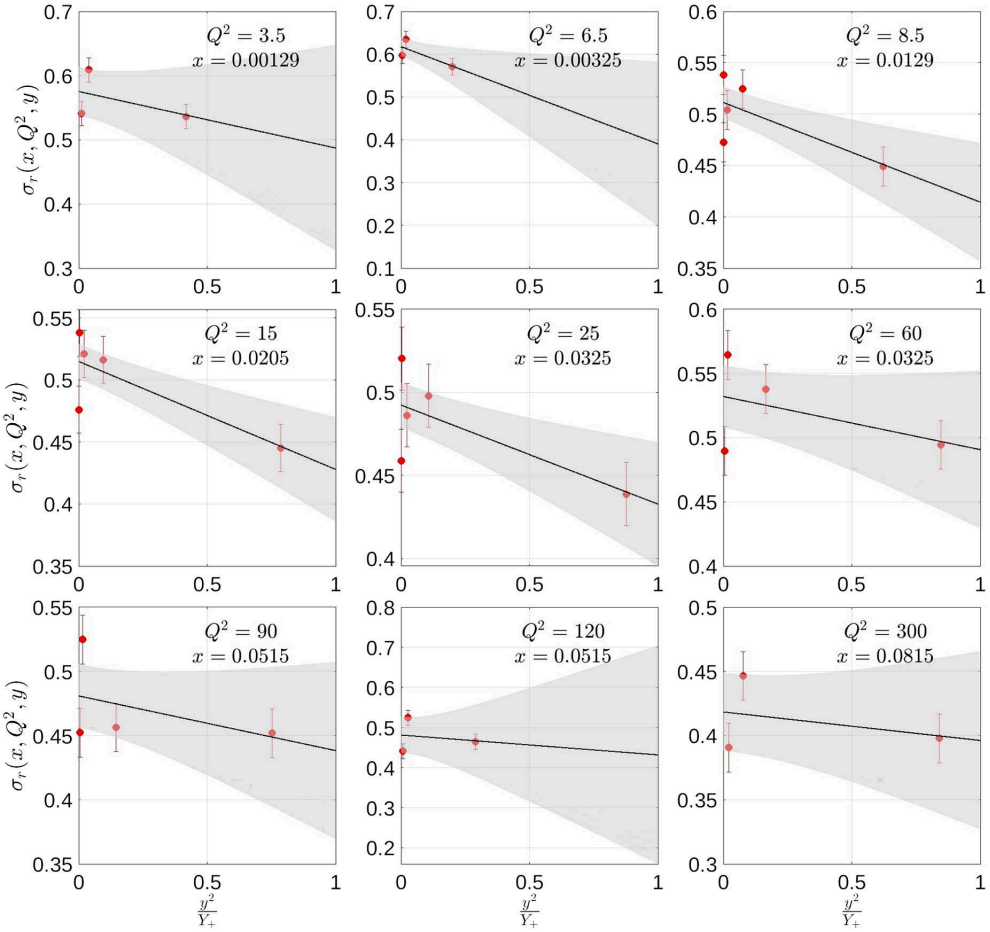

FIG. 1. Results of the fitting procedure for nine example x and Q^2 values in the conservative scenario. The simulated reduced cross section measurements are shown in red, where each point corresponds to a different center-of-mass energy and the vertical error bars represent the total uncertainties described in Sec. III. The 68% confidence bands for each fit are depicted in light gray. Note that there is a suppressed zero on the vertical axis.

randomly smeared using samples from Gaussian distributions that reflect the assumed experimental uncertainties.

Two different scenarios are considered. The first, referred to here as the "conservative scenario," is based largely on the systematic precision achieved at HERA, and follows the considerations in [20], as also adopted in the studies by ATHENA collaboration, and subsequently used to study EIC collinear PDF sensitivities [21] and α_s measurements [37]. In the moderate y range studied here, the data points have a point-to-point uncorrelated systematic uncertainty of 1.9%. A normalization uncertainty of 3.4% is also included for each dataset, which is not correlated between different beam energy configurations, such that the total uncertainty attributed to each data point is 3.9%. More recent estimates of the achievable EIC precision suggest that a much better performance will be obtained than that in the conservative scenario. There is also expected to be some correlation between the normalization uncertainties at different beam energies. We therefore also consider a second "optimistic" scenario, which follows the assumption in [38] that the total uncertainty that is uncorrelated between data points at different beam energies is 1%. At the time of writing, the rather different assumptions in the conservative and optimistic scenarios can be seen as extreme cases, with the final achieved precision likely to lie between them.

III. EXTRACTION OF F_L

The neutral current (NC) $e^{\pm}p$ DIS cross sections are given by a linear combination of generalized structure functions [1]. For $Q^2 \ll M_Z^2$ (mass of the Z boson squared),

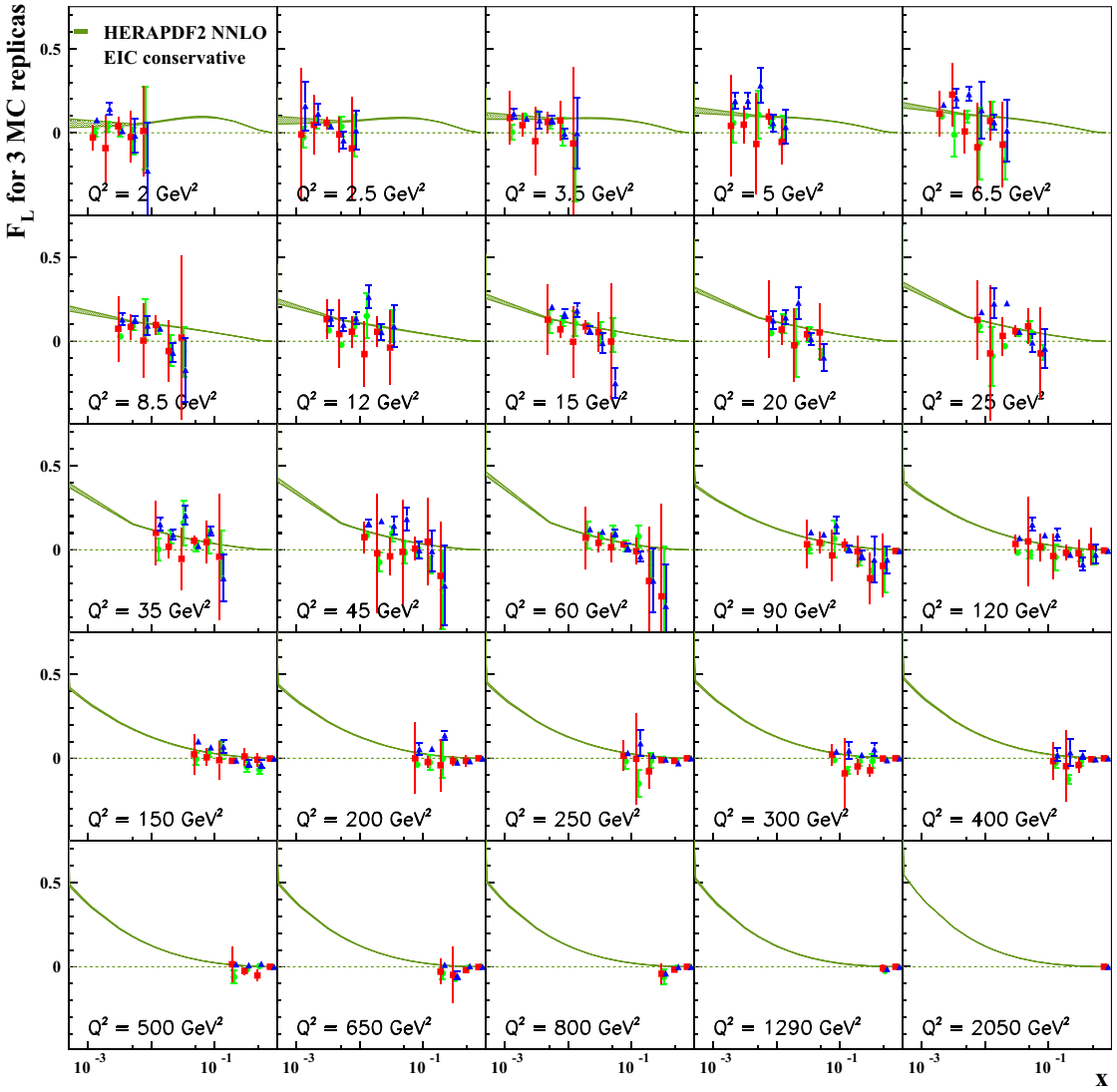

FIG. 2. Simulated extractions of the longitudinal structure function F_L for three different pseudodata replicas in the conservative scenario, with different colors corresponding to different replicas, whose x positions are slightly shifted for visibility. The theoretical predictions from HERAPDF2.0 NNLO are also shown as bands whose widths correspond to the uncertainties on the predictions.

the inclusive cross section for NC DIS can be written in terms of the two structure functions F_L and F_2 as

$$\frac{\mathrm{d}^2\sigma^{e^\pm p}}{\mathrm{d}x\mathrm{d}Q^2} = \frac{2\pi\alpha^2 Y_+}{xQ^4}\left[F_2(x,Q^2) - \frac{y^2}{Y_+}F_L(x,Q^2)\right] = \frac{2\pi\alpha^2 Y_+}{xQ^4}\sigma_r(x,Q^2,y), \quad (1)$$

where α is the fine structure constant, $Y_+ = 1 + (1-y)^2$, and σ_r is usually referred to as the reduced cross section.

Equation (1) implies that there is a linear relationship between the reduced cross section and y^2/Y_+, which is a function only of the inelasticity of the process, adjustable at fixed x and Q^2 by changing the center-of-mass energy and exploiting the relationship $Q^2 \simeq sxy$. Using measurements of σ_r at different s, the values of F_2 and F_L can thus be separately obtained in a model-independent way as the free parameters of a linear fit. This Rosenbluth-type separation technique [39] has been employed in fixed-target data and at HERA and has also recently been applied to the extraction of the diffractive longitudinal structure function at the EIC [38]. For each (x, Q^2), we thus apply a fit of the form

$$\sigma_r(x,Q^2,y) = F_2(x,Q^2) - \frac{y^2}{Y_+}F_L(x,Q^2), \quad (2)$$

where $F_2(x,Q^2)$ and $F_L(x,Q^2)$ are free parameters, obtained through a χ^2 minimization implemented in Python using SciPy [40]. Equation (1) can also be fitted using a Bayesian method to obtain F_L, as done by ZEUS

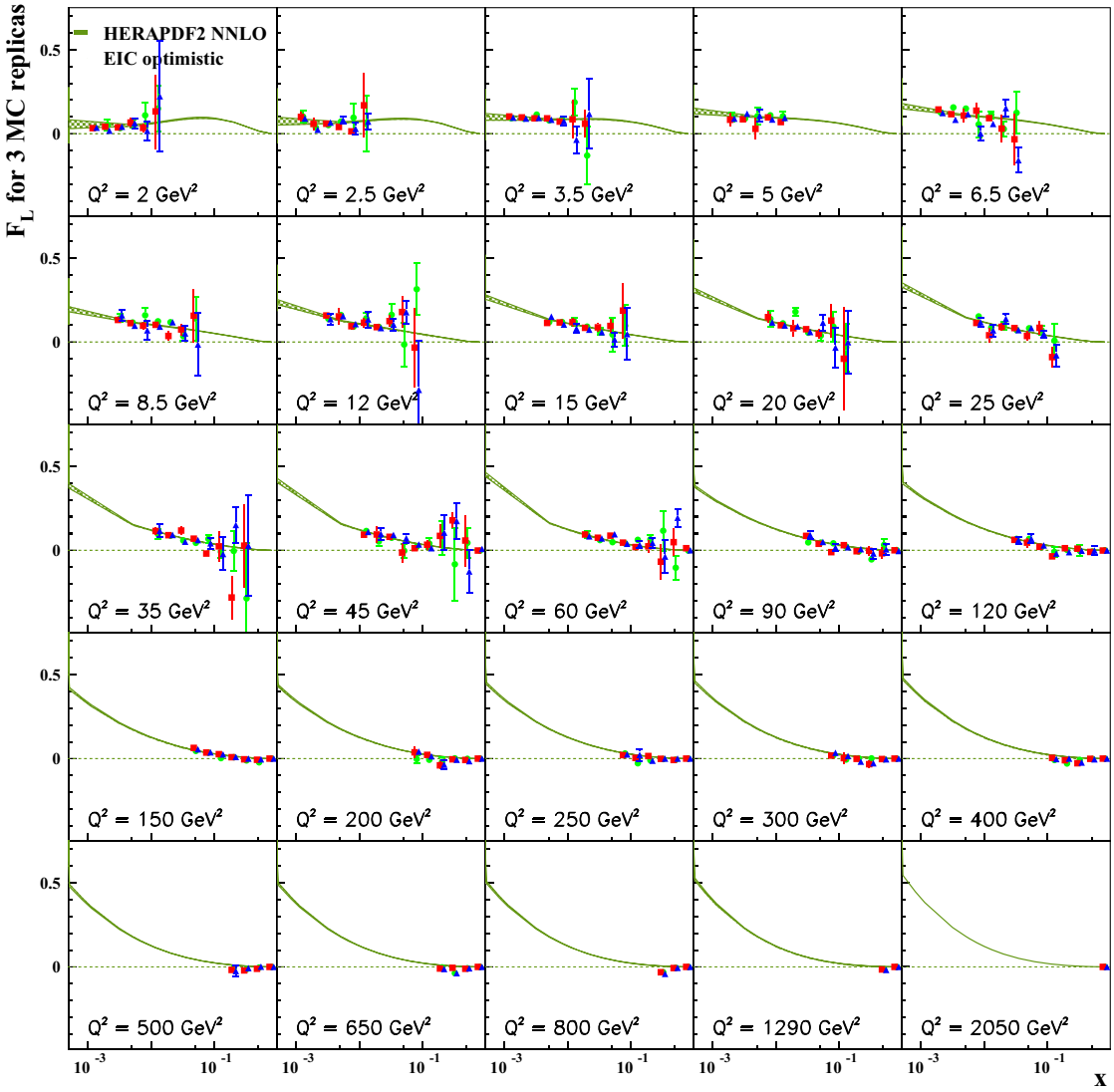

FIG. 3. Simulated extractions of the longitudinal structure function F_L for three different pseudodata replicas in the optimistic scenario, with different colors corresponding to different replicas, whose x positions are slightly shifted for visibility. The theoretical predictions from HERAPDF2.0 NNLO are also shown as bands whose widths correspond to the uncertainties on the predictions.

Collaboration [11]. We used the BAT package [41] to cross-check the results using this method, obtaining perfect agreement.

Figure 1 depicts fits in the conservative scenario at nine example values of x and Q^2, together with the 68% confidence bands for each fit. Due to the details of the binning scheme adopted here, the range in y^2/Y_+ varies substantially between bins. Different combinations of Q^2 and x lead to data points within the acceptable y range at three, four, or five different $\sqrt{s}$ values. For Q^2 and x combinations with less than three such data points, no extraction of F_L is attempted.

The pseudodata smearing procedure introduces randomness into the fit inputs, which is reflected in the outputs as fluctuations in both the extracted F_L values and their uncertainties, which are obtained from variations of the parameter resulting in a $\Delta\chi^2 = 1$. The F_L uncertainty results are, therefore, samples from distributions of possible outcomes, which are often quite broad. In order to sample the distribution of possible uncertainty outcomes in a more systematic way, we adopt the method introduced in [38] and further described in Sec. IV B, whereby the results are averaged over multiple replicas of the procedure. With sufficiently large numbers of replicas (1000 is used by

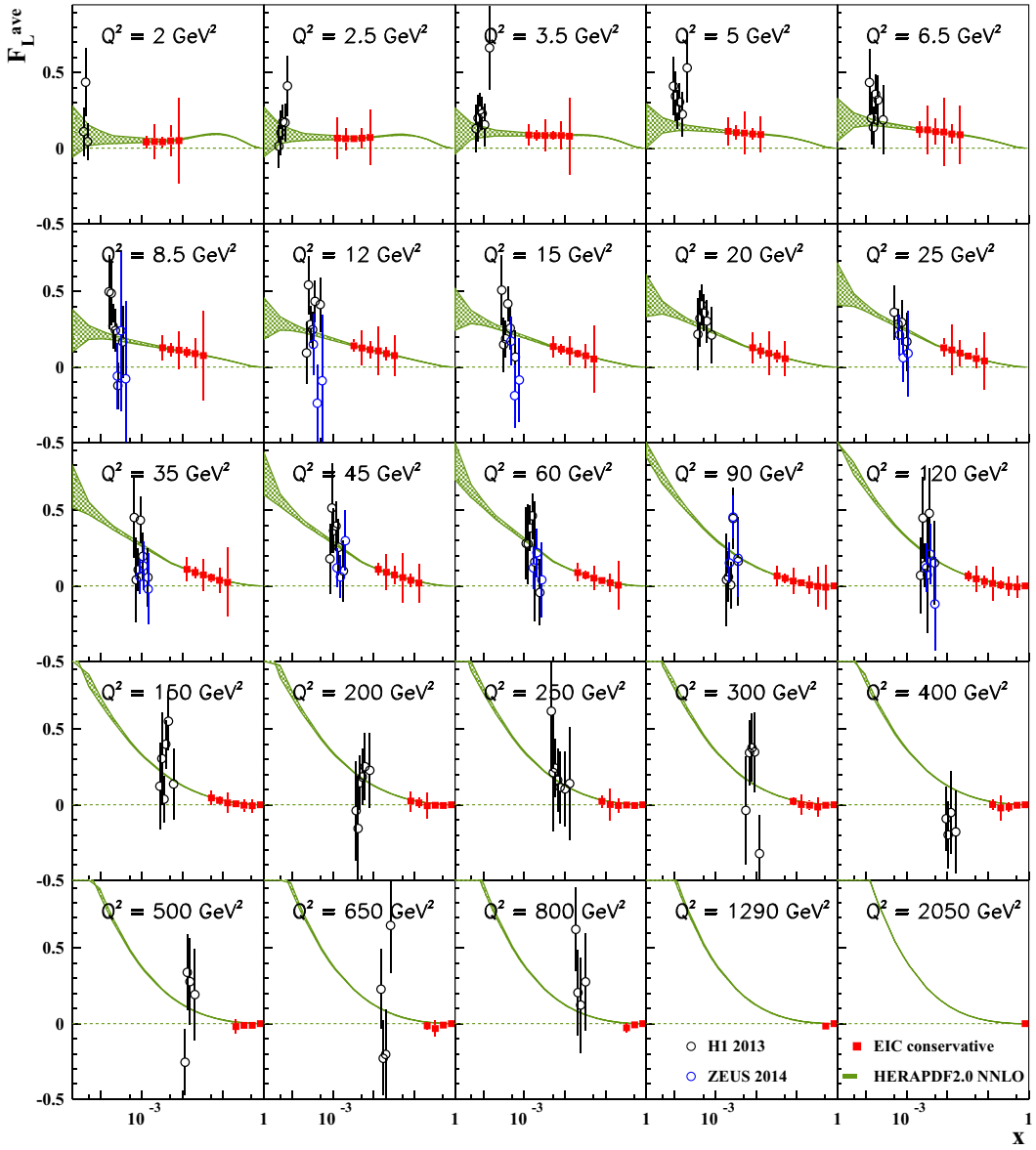

FIG. 4. Simulated extractions of the longitudinal structure function F_L averaged over 1000 replicas for the conservative EIC uncertainty scenario, shown together with data from H1 and ZEUS collaborations, alongside the theoretical predictions from HERAPDF2.0 NNLO. The error bars on the points represent the total experimental uncertainties, while the widths of the bands correspond to the uncertainties on the theoretical predictions.

default), both the mean and the variance tend toward results that can be considered as expectation values for the simulated scenario.

In the following sections, we only consider bins where the absolute uncertainty of F_L averaged over the 1000 replicas is smaller than 0.3. This choice results in more data points surviving in the optimistic than the conservative scenario since the overall level of the uncertainties is smaller. Particularly for small Q^2, it also tends to exclude some data points at high x with large uncertainties that might be recovered in a future analysis. This criterion removes about 30% of points for the realistic scenario and 20% for the optimistic one.

IV. RESULTS

A. Example F_L replicas

To sample the distribution of possible outcomes for the expected values and uncertainties on F_L in a statistically meaningful way, we performed the smearing and fitting procedures described in Secs. II and III multiple times, leading to a set of replica results, each of which is an independently created pseudodata set. Figures 2 and 3 show the resulting longitudinal structure function F_L overlaid for three randomly chosen example replicas, for the conservative and optimistic scenarios, respectively.

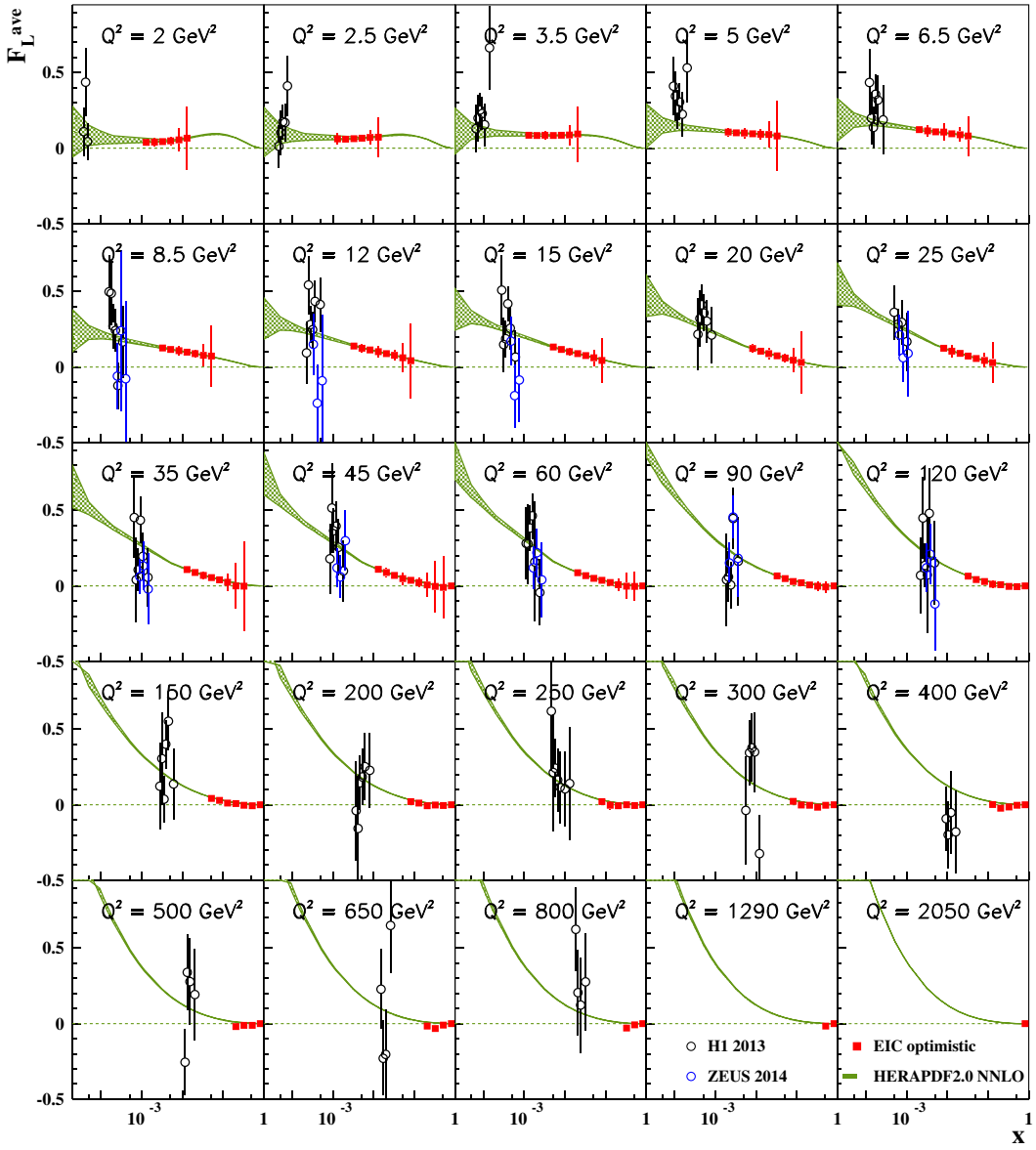

FIG. 5. Simulated extractions of the longitudinal structure function F_L averaged over 1000 replicas for the optimistic EIC uncertainty scenario, shown together with data from H1 and ZEUS collaborations, alongside the theoretical predictions from HERAPDF2.0 NNLO. The error bars on the points represent the total experimental uncertainties, while the widths of the bands correspond to the uncertainties on the theoretical predictions.

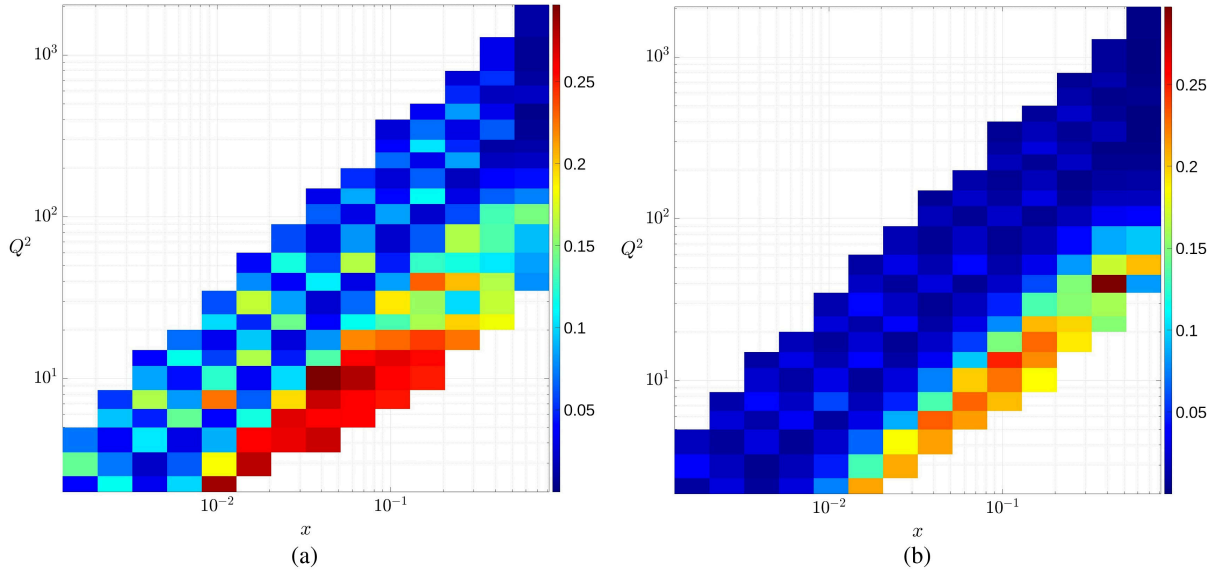

FIG. 6. Uncertainties on the simulated EIC F_L measurements averaged over 1000 replicas. Image (a) corresponds to the conservative scenario and (b) to the optimistic scenario, with the colors indicating the absolute uncertainties with the same scale in both cases. Points in x and Q^2 for which the absolute uncertainty on F_L is larger than 0.3 are not shown.

The spread between different replicas, arising from the random smearing of the reduced cross section data to simulate their uncertainties, propagates into the F_L pseudodata, leading to substantially more precise results and a smaller spread between replicas in the optimistic than in the conservative scenario. The theoretical predictions calculated with the HERAPDF2.0 NNLO set are also shown in the figures, and describe the pseudodata well by construction.

B. Averaging over F_L replicas

To obtain a robust expectation for the predicted uncertainties on F_L, we used the averaging procedure described in [38], which yields a single pseudodata point for F_L at each x and Q^2 value, averaged over 1000 replicas. The average and variance were calculated as

$$\bar{v} = \frac{S_1}{N}, \quad (\Delta v)^2 = \frac{S_2 - S_1^2/N}{N-1}, \tag{3}$$

where $S_n = \sum_{i=1}^{N} v_i^n$ and v_i is the value of F_L in the i-th MC sample. The results are shown in Figs. 4 and 5 for the conservative and optimistic scenarios, respectively. The fluctuations in the uncertainties between neighboring data points reflect the variations in the numbers of bins and their y^2/Y_+ ranges included in the Rosenbluth separation fits, as illustrated in Fig. 1. A smoother response could be achieved with a modified binning scheme for the input pseudodata at each $\sqrt{s}$, for example a switch from an (x, Q^2) to a (y, Q^2) grid.

The uncertainties on the averaged points, which can now be taken as a measure of the expected precision, can be compared with the uncertainties on the theoretical predictions, which are indicated through the widths of the corresponding bands and are driven primarily by the uncertainty on the gluon density in the HERAPDF2.0 PDF set. In the optimistic scenario, the precision of the pseudodata is comparable to that of the theoretical predictions at low and intermediate Q^2, suggesting that such a measurement would provide a direct constraint that significantly improves our knowledge of the gluon density in the proton. Although this is not so evidently the case in the conservative scenario, the data would still be a useful ingredient in fits, as well as providing a test of the consistency of the overall PDF framework.

Measurements by H1 [10] and ZEUS [11] collaborations are also shown[1] alongside the simulated EIC data in Figs. 4 and 5. The EIC data sample a region of x between one and two orders of magnitude higher than the HERA measurements, and also extend to larger Q^2, ultimately reaching regions where the predicted F_L values become very small. In both the optimistic and the conservative scenarios, the expected precision of the EIC pseudodata is very much better than that of the HERA data, a consequence of the much larger assumed integrated luminosities and the larger number of $\sqrt{s}$ values in the Rosenbluth fits. These figures illustrate that in both uncertainty scenarios, the EIC will measure the longitudinal structure function in a kinematic

[1]Some of the ZEUS data points have slightly different Q^2 values from the H1 measurements, which are adopted here. The ZEUS data points have, therefore, been adjusted to the H1 Q^2 values using factors obtained from HERAPDF2.0 NNLO. These factors were small, not exceeding 4%.

region that is complementary to that accessed at HERA and with a much improved precision.

In Fig. 6, the expected precision on each F_L data point is shown in the conservative and optimistic scenarios after carrying out the averaging procedure in Eq. (3). The overall size of the uncertainties scales approximately linearly with the systematic uncertainty assumptions in the two scenarios. Absolute values of the uncertainties at the level of 0.05 are obtained across a wide kinematic range in the optimistic scenario, corresponding to around 20% precision, where F_L itself is relatively large. As can be seen in Fig. 4, the HERA measurements have much larger uncertainties, in excess of 100% for over half of the data points. At the largest x values, the quality of the simulated EIC measurements deteriorates, as the lever arm in y^2/Y_+ gets shorter. Bin-to-bin fluctuations are visible in the uncertainties, following similar patterns between the optimistic and conservative scenarios, once again corresponding to the varying conditions in terms of numbers of data points and their y^2/Y_+ ranges, as illustrated in Fig. 1.

C. Averaging F_L over x

The HERA F_L measurements are often presented as a function of Q^2 after averaging over x. To compare the simulated EIC data in this projection, the F_L pseudodata averaged over the 1000 replicas were further averaged over all x values at each Q^2 using a simple weighted-mean procedure, where the weights are derived from the uncertainties in each F_L measurement. The data are attributed to an averaged value of x, obtained using the same weights as for the F_L averaging.

The results for $F_L(Q^2)$ in the conservative scenario are shown in Fig. 7(a), together with the average values of x and the theoretical predictions based on HERAPDF2.0 NNLO. For Q^2 values larger than around 100 GeV^2, the values of F_L become very small at the x values considered. The agreement of the pseudodata and the predictions is very good, as expected by construction. The data are presented alongside an equivalent figure showing the HERA data [10], with the axis scales chosen to be equivalent to allow a direct comparison between the Q^2 ranges and the level of precision. Even for the conservative scenario shown here, the uncertainties on the EIC measurements are significantly smaller than those on the HERA data. The magnitude of F_L for the EIC data points is always smaller than that from HERA at the same Q^2 value, due to the dependence of F_L on x and the larger x values sampled at EIC compared with HERA. It is clear that the EIC will be able to measure the longitudinal structure function F_L with unprecedented precision and in so far unexplored kinematic regions.

V. ALTERNATIVE SCENARIOS

Since the running schedule over time for the EIC is still far from certain, we have studied the influence of different

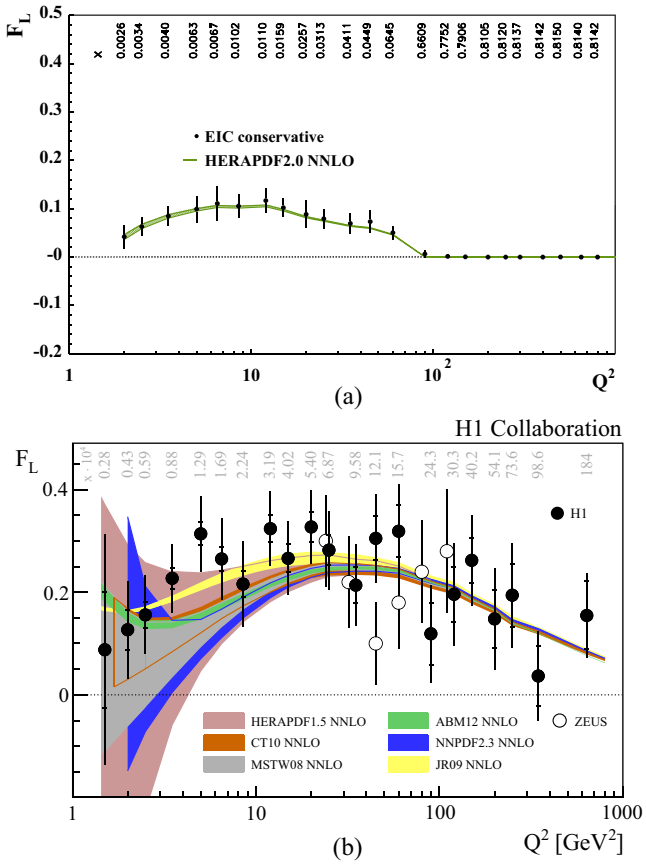

FIG. 7. (a) Simulated EIC measurements of the longitudinal structure function F_L in the conservative scenario, averaged over 1000 replicas, shown as a function of Q^2 and compared with the theoretical prediction given by HERAPDF2.0 NNLO. (b) Summary plot for existing HERA measurements of F_L averaged over x and compared with predictions at NNLO from various PDF sets [10]. The horizontal and vertical scales in (a) and (b) are chosen to be identical for ease of comparison, and in both cases the weighted-average x value is indicated for each data point.

aspects, which may be helpful as input to the decision-making process. In addition to the influence of the systematic uncertainties, as studied in Sec. IV through the difference between the optimistic and conservative scenarios, it is also interesting to investigate the influence of statistical uncertainties by varying the integrated luminosity assumed for each of the different beam energy and $\sqrt{s}$ configurations. In place of the annual luminosities for each case assumed by default (Table I), we have therefore repeated the full study with only 1 fb^{-1} for each of the beam energies. Although only a small fraction of the peak luminosities expected for EIC, this is larger than the total sample sizes obtained at HERA and may be a realistic EIC target for early running, or for a dedicated running period with frequent beam energy changes targeting physics studies, such as that presented here for F_L.

The expected precision on the F_L extraction as a function of Q^2 is compared for the different systematic and statistical

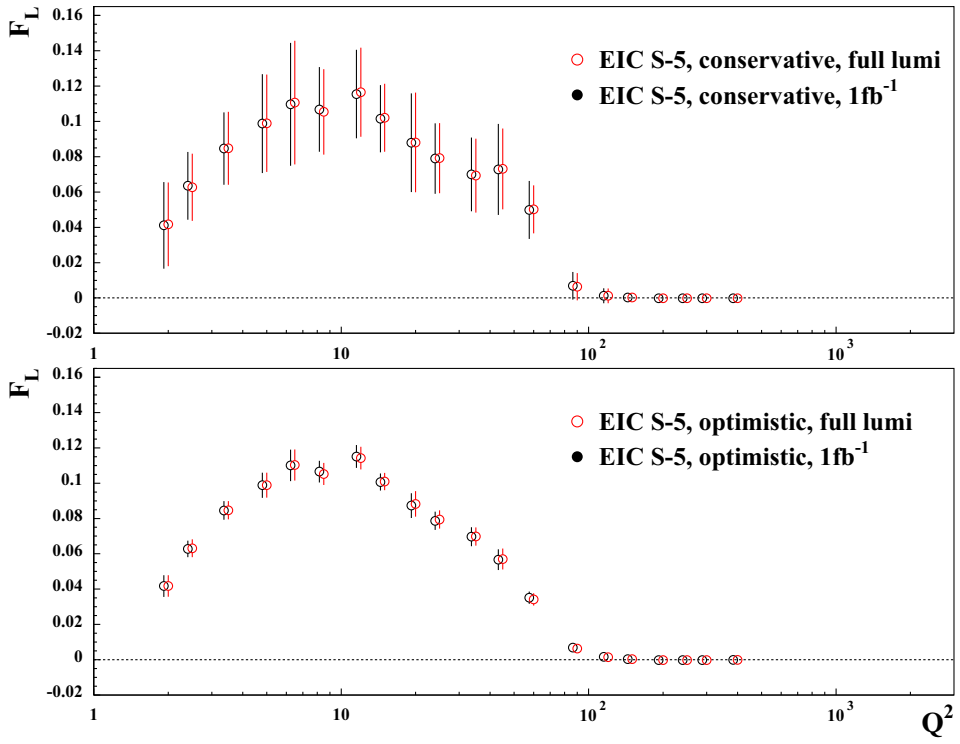

FIG. 8. Simulated $F_L(Q^2)$ data based on five beam energy configurations in the conservative (top) and optimistic (bottom) scenarios. In both cases, comparisons are made between results, assuming a full nominal year of integrated luminosity in each configuration (Table I) and a scenario in which 1 fb^{-1} is assumed for each configuration. The data points with the different luminosity assumptions are slightly offset from one another for visibility.

uncertainty scenarios in Fig. 8. As for the two-dimensional projections, there is a difference of a factor of around 3–4 between the results with the conservative and optimistic scenarios, with the assumed uncertainties propagating approximately linearly. The influence of reducing the integrated luminosity is minor by comparison, confirming that 1 fb^{-1} at each $\sqrt{s}$ is more than sufficient to achieve the required level of statistical precision and ensure that the F_L extraction is systematically limited, even in the optimistic scenario with 1% systematics.

We have additionally investigated the potential to improve the precision on F_L by increasing the number of beam energy configurations and hence $\sqrt{s}$ values in the Rosenbluth decompositions. Following [21], in addition to the default scenario with five configurations (referred to in the following as S-5), we have also considered different combinations of the same sets of electron and proton beam energies that lead to different $\sqrt{s}$ values. As illustrated in Table II, we consider scenarios with nine (S-9) or 17 (S-17) different configurations. Not all of the combinations considered are necessarily technically realizable at the EIC, so the choices made here should be considered only as indicative, chosen in order to explore the potential improvements that might be achievable.

Results with the different numbers of beam configurations are compared at the level of the Rosenbluth fits for a typical example bin in x and Q^2 in Fig. 9 in the conservative scenario. The larger number of beam energy configurations leads both to an increase in the number of data points available for the fits and to an extended lever arm for the fit. For the example bin shown, the uncertainty on F_L decreases by a factor of approximately three between the S-5 and S-9 scenarios and by a further factor of around two when extending to the full S-17 case.

As noted in Sec. IV A, our method leads to bin-to-bin fluctuations in the uncertainties on the extracted F_L due to the differences between the number of accessible points

TABLE II. Center-of-mass energies (in GeV) for various combinations of electron and proton beam energies. The default case studied here (S-5) with five configurations is indicated in italics. Additional combinations introduced in the S-9 scenario are in bold. For the S-17 scenario, the full set of combinations is included, except for the degenerate case at $\sqrt{s} = 85$ GeV (in parentheses).

		E_p [GeV]					
		41	100	120	165	180	275
E_p [GeV]	5	*29*	*45*	49	**57**	60	74
	10	40	*63*	69	**81**	(85)	*105*
	18	54	**85**	93	**109**	114	*141*

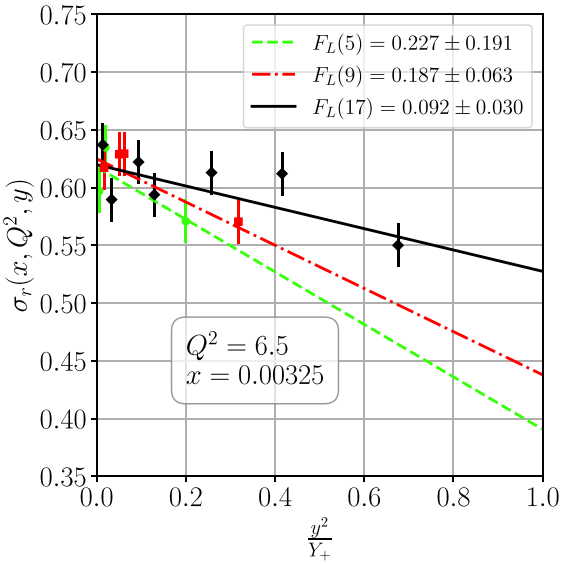

FIG. 9. Comparison of Rosenbluth decomposition fits to simulated EIC data in an example bin defined by $Q^2 = 6.5\ \mathrm{GeV}^2$ and $x = 0.00325$ under three different assumptions as to the beam energy configurations that are included. The points shown in green are available in the S-5 scenario, and correspond to the fit shown as the green line and the result indicated as "$F_L(5)$." Additional points that become available in the S-9 scenario are shown in red, with the corresponding fit to the green and red points shown in red and indicated as "$F_L(9)$." The black points are introduced in the S-17 scenario, with the black line and the "$F_L(17)$" result corresponding to a fit to all points shown.

and their y^2/Y_+ ranges as x and Q^2 are varied. This is reflected in the improvements in the uncertainties in the two-dimensional projections as more $\sqrt{s}$ values are added, with some bins unaffected and others showing substantial improvements. An additional region of phase space at low y also becomes accessible with reasonable precision. The impact of the additional beam energy configurations is illustrated at the level of the x-averaged dependence of F_L on Q^2 in Fig. 10 for both the optimistic and the conservative scenarios. The bin-to-bin fluctuations in the uncertainties are smoothed out to a large extent in the averaging procedure. Significant improvements are visible in the precision both when increasing the number of configurations from the S-5 to the S-9 set and also from S-9 to S-17. This remains the case for both the optimistic and the conservative scenarios, though the introduction of more configurations is not sufficient to compensate for the difference between the two rather different uncertainty scenarios. In these figures, the averaged F_L values are different in the different scenarios, since adding new points in the Rosenbluth fits alters the selection of F_L data points passing the uncertainty criteria for inclusion in the figures and the uncertainties on each individual point, leading to changes in the weighted-average values of x.

The simple studies performed in this section represent only a small fraction of the total range of possible variations that could be studied, and further optimization is, therefore, certainly possible. Nevertheless, it is clear that minimizing the systematic uncertainties on the data is the single most important ingredient in obtaining high precision on F_L, and that a dedicated running period with lots of beam energy configurations and modest luminosities is a possible approach to obtaining a high-quality result with a relatively small amount of EIC beam time.

VI. SUMMARY AND CONTEXT

In this work, we have explored the potential of the EIC to measure the longitudinal structure function F_L using simulated data. Our studies indicated that the EIC will

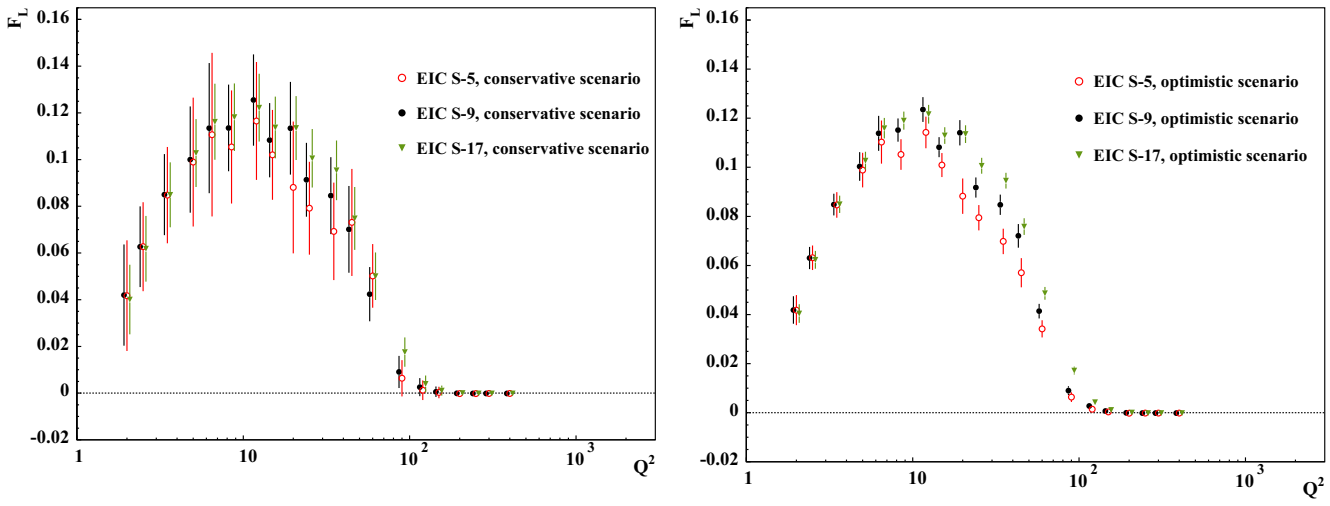

FIG. 10. Comparison between simulated EIC $F_L(Q^2)$ results averaged over x and shown as a function of Q^2 in the S-5, S-9, and S-17 scenarios regarding beam energy combinations. The conservative assumption on systematic precision is shown on the left, with the optimistic scenario on the right. Data points from the different scenarios are slightly shifted relative to one another for visibility.

be able to measure $F_L(x, Q^2)$ with an unprecedented precision over a wide kinematic range. In scenarios with the most favorable assumptions, absolute uncertainties of less than 0.05 are achievable across a wide kinematic range, corresponding to around 20% where F_L is largest and offering competitive constraints on the proton gluon density. This represents a significant improvement compared with HERA, which was sensitive to a region where F_L is larger than at EIC, but where the most precise results from double-differential cross sections in x and Q^2 have uncertainties of around of 30%–40%, and where around 30% of all measurements have uncertainties larger than 100%. No attempt has been made to optimize the binning schemes used here. Refinements, for example by adopting a (y, Q^2) instead of a (x, Q^2) grid to optimally populate the y^2/Y_+ range in the Rosenbluth decomposition fits, are expected to lead to improved precision and to the addition of further bins at low Q^2 and high x that are kinematically accessible but excluded in the current analysis on the basis of having very large uncertainties on F_L.

By making variations in the analysis details, we have investigated the impact of different qualities of measurement and choices of EIC running plan. The most striking dependence is on the magnitude of the systematic uncertainties that are not correlated between different $\sqrt{s}$ values at the same x and Q^2. The rather aggressive 1% "optimistic" assumption for such uncertainties that was studied here may not to be ultimately achievable, but it is reasonable to expect the final EIC situation to be much closer to 1% than to the "conservative" 3.9% scenario that was also investigated. By comparison with the systematics, statistical uncertainties play a much more minor role—a reflection of the fact that F_L is obtained from inclusive measurements and the large expected sample sizes at the EIC. If the initial assumption of a year of running at each beam energy is drastically reduced to an example of 1 fb^{-1} for each of the five beam energy configurations, the expected precision on F_L is not substantially deteriorated. On the other hand, a significant advantage can be gained by adding more beam energy configurations, which leads to more data points in the Rosenbluth decomposition fits spanning a wider range in the relevant y^2/Y_+ variable. The precision improves progressively when studying cases in which either nine or 17 configurations are included in place of the default five. Running scenarios with relatively low luminosities collected at relatively large numbers of different $\sqrt{s}$ values seem to be the most efficient in terms of precision on F_L.

The kinematic region that is accessible with EIC data is complementary to that of HERA, covering a region of larger x and also extending to higher Q^2. The coverage of the EIC data is placed in the wider context of world F_L data, also including fixed-target measurements, in Fig. 11. The EIC data close the large current gap between the fixed-target and the HERA data. This is already the case in the scenario with five $\sqrt{s}$ values (S-5), but the extension to nine configurations (S-9) yields additional data points at large Q^2, leading to a rather complete coverage of the kinematic plane overall for $Q^2 > 1\ \text{GeV}^2$, extending as low as $x \sim 10^{-4}$ and approaching the situation for F_2. Altogether, the EIC has the potential to transform our knowledge of F_L across a wide kinematic range, potentially leading to a substantial impact on the precision on the proton PDFs and constraining phenomenological models in new ways.

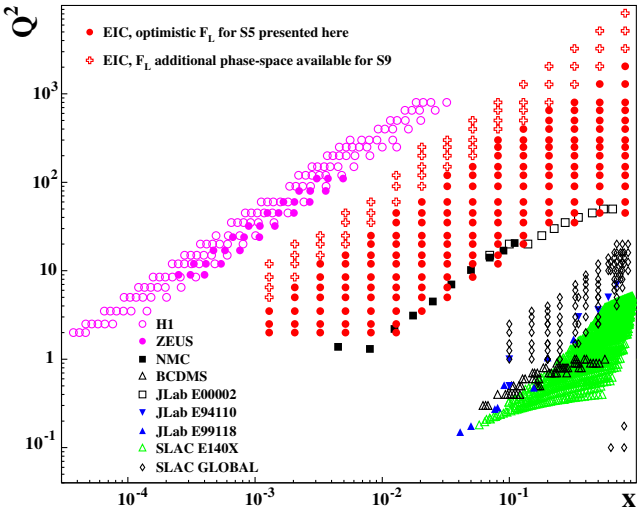

FIG. 11. Kinematic coverage of world data for the proton longitudinal structure function, derived from Fig. 1 in [17], but with simulated EIC data added. The existing data shown are from H1 and ZEUS [10,11], NMC [13], BCDMS [12], JLab [15,17,18], and SLAC [14,16]. The EIC pseudodata are shown in the S-5 and S-9 scenarios, which correspond to five and nine different beam energy configurations, respectively.

ACKNOWLEDGMENTS

Much of the analysis framework used here has evolved from collaboration with Nestor Armesto, Anna Stąśto, and Wojtek Słomiński, to whom we are grateful. We would also like to thank Oliver Schulz for his help with the BAT package. J. J.-L. acknowledges the DESY Summer Student Program for significantly contributing to the development of this work.

DATA AVAILABILITY

No data were created or analyzed in this study.

[1] R. Devenish and A. Cooper-Sarkar, *Deep Inelastic Scattering* (Oxford University Press, New York, 2003).

[2] H. Abramowicz *et al.* (H1 and ZEUS Collaborations), Combination of measurements of inclusive deep inelastic $e^{\pm}p$ scattering cross sections and QCD analysis of HERA data, Eur. Phys. J. C **75**, 580 (2015).

[3] S. Alekhin, J. Blümlein, S. Moch, and R. Placakyte, Parton distribution functions, α_s, and heavy-quark masses for LHC Run II, Phys. Rev. D **96**, 014011 (2017).

[4] T.-J. Hou *et al.*, New CTEQ global analysis of quantum chromodynamics with high-precision data from the LHC, Phys. Rev. D **103**, 014013 (2021).

[5] S. Bailey, T. Cridge, L. A. Harland-Lang, A. D. Martin, and R. S. Thorne, Parton distributions from LHC, HERA, Tevatron and fixed target data: MSHT20 PDFs, Eur. Phys. J. C **81**, 341 (2021).

[6] R. D. Ball *et al.* (NNPDF Collaboration), The path to proton structure at 1% accuracy, Eur. Phys. J. C **82**, 428 (2022).

[7] A. M. Cooper-Sarkar, G. Ingelman, K. R. Long, R. G. Roberts, and D. H. Saxon, Measurement of the longitudinal structure function and the small x gluon density of the proton, Z. Phys. C **39**, 281 (1988).

[8] G. R. Boroun and B. Rezaei, Analysis of the proton longitudinal structure function from the gluon distribution function, Eur. Phys. J. C **72**, 2221 (2012).

[9] E. B. Zijlstra and W. L. van Neerven, Order $\alpha_s{}^2$ QCD corrections to the deep inelastic proton structure functions F_2 and F_L, Nucl. Phys. **B383**, 525 (1992).

[10] V. Andreev *et al.* (H1 Collaboration), Measurement of inclusive ep cross sections at high Q^2 at $\sqrt{s} = 225$ and 252 GeV and of the longitudinal proton structure function F_L at HERA, Eur. Phys. J. C **74**, 2814 (2014).

[11] H. Abramowicz *et al.* (ZEUS Collaboration), Deep inelastic cross-section measurements at large y with the ZEUS detector at HERA, Phys. Rev. D **90**, 072002 (2014).

[12] A. Benvenuti *et al.*, A high statistics measurement of the proton structure functions $F_2(x, Q^2)$ and R from deep inelastic muon scattering at high Q^2, Phys. Lett. B **223**, 485 (1989).

[13] M. Arneodo *et al.*, Measurement of the proton and deuteron structure functions, F_2^p and F_2^d, and of the ratio σ_L/σ_T, Nucl. Phys. **B483**, 3 (1997).

[14] E140X Collaboration, Precision measurement of $R = \sigma_L/\sigma_T$ on hydrogen, deuterium and beryllium targets in deep inelastic electron scattering, Z. Phys. C **70**, 387 (1996).

[15] V. Tvaskis *et al.*, Longitudinal-transverse separations of structure functions at low Q^2 for hydrogen and deuterium, Phys. Rev. Lett. **98**, 142301 (2007).

[16] L. W. Whitlow, E. M. Riordan, S. Dasu, S. Rock, and A. Bodek, Precise measurements of the proton and deuteron structure functions from a global analysis of the SLAC deep inelastic electron scattering cross-sections, Phys. Lett. B **282**, 475 (1992).

[17] V. Tvaskis *et al.*, Measurements of the separated longitudinal structure function F_L from hydrogen and deuterium targets at low Q^2, Phys. Rev. C **97**, 045204 (2018).

[18] Y. Liang *et al.* (Jefferson Lab Hall C E94-110 Collaboration), Measurement of $R = \sigma_L/\sigma_T$ and the separated longitudinal and transverse structure functions in the nucleon-resonance region, Phys. Rev. C **105**, 065205 (2022).

[19] A. Accardi *et al.*, Electron-Ion Collider: The next QCD frontier: Understanding the glue that binds us all, Eur. Phys. J. A **52**, 268 (2016).

[20] R. Abdul Khalek *et al.*, Science requirements and detector concepts for the Electron-Ion Collider: EIC Yellow report, Nucl. Phys. **A1026**, 122447 (2022).

[21] N. Armesto, T. Cridge, F. Giuli, L. Harland-Lang, P. Newman, B. Schmookler, R. Thorne, and K. Wichmann, Impact of inclusive electron ion collider data on collinear parton distributions, Phys. Rev. D **109**, 054019 (2024).

[22] J. Adam *et al.* (ATHENA Collaboration), ATHENA detector proposal—a totally hermetic electron nucleus apparatus proposed for IP6 at the Electron-Ion Collider, J. Instrum. **17**, P10019 (2022).

[23] J. K. Adkins *et al.*, Design of the ECCE detector for the Electron Ion Collider, Report No. jLAB-PHY-24-4124, 2022, arXiv:2209.02580.

[24] S. Alekhin *et al.*, HERAFitter, Eur. Phys. J. C **75**, 304 (2015).

[25] F. D. Aaron *et al.* (H1 and ZEUS Collaborations), Combined measurement and QCD analysis of the inclusive $e^{\pm}p$ scattering cross sections at HERA, J. High Energy Phys. 01 (2010) 109.

[26] F. D. Aaron *et al.* (H1 Collaboration), A precision measurement of the inclusive ep scattering cross section at HERA, Eur. Phys. J. C **64**, 561 (2009).

[27] V. N. Gribov and L. N. Lipatov, Deep inelastic ep scattering in perturbation theory, Sov. J. Nucl. Phys. **15**, 438 (1972).

[28] V. N. Gribov and L. N. Lipatov, e^+e^- pair annihilation and deep inelastic ep scattering in perturbation theory, Sov. J. Nucl. Phys. **15**, 675 (1972).

[29] L. N. Lipatov, The parton model and perturbation theory, Yad. Fiz. **20**, 181 (1974).

[30] Y. L. Dokshitzer, Calculation of the structure functions for deep inelastic scattering and e^+e^- annihilation by perturbation theory in quantum chromodynamics, Sov. Phys. JETP **46**, 641 (1977).

[31] G. Altarelli and G. Parisi, Asymptotic freedom in parton language, Nucl. Phys. **B126**, 298 (1977).

[32] S. Moch, J. A. M. Vermaseren, and A. Vogt, The three-loop splitting functions in QCD: The non-singlet case, Nucl. Phys. **B688**, 101 (2004).

[33] A. Vogt, S. Moch, and J. A. M. Vermaseren, The three-loop splitting functions in QCD: The singlet case, Nucl. Phys. **B691**, 129 (2004).

[34] A. A. Almasy, S. Moch, and A. Vogt, On the next-to-next-to-leading order evolution of flavour-singlet fragmentation functions, Nucl. Phys. **B854**, 133 (2012).

[35] A. Mitov, S. Moch, and A. Vogt, Next-to-next-to-leading order evolution of non-singlet fragmentation functions, Phys. Lett. B **638**, 61 (2006).

[36] J. Blümlein, P. Marquard, C. Schneider, and K. Schönwald, The three-loop unpolarized and polarized non-singlet anomalous dimensions from off shell operator matrix elements, Nucl. Phys. **B971**, 115542 (2021).

[37] S. Cerci, Z. S. Demiroglu, A. Deshpande, P. R. Newman, B. Schmookler, D. S. Cerci, and K. Wichmann, Extraction of the strong coupling with HERA and EIC inclusive data, Eur. Phys. J. C **83**, 1011 (2023).

[38] N. Armesto, P. R. Newman, W. Słomiński, and A. M. Staśto, Diffractive longitudinal structure function at the Electron Ion Collider, Phys. Rev. D **105**, 074006 (2022).

[39] M. N. Rosenbluth, High energy elastic scattering of electrons on protons, Phys. Rev. **79**, 615 (1950).

[40] P. Virtanen *et al.*, SciPy 1.0–Fundamental algorithms for scientific computing in Python, Nat. Methods **17**, 261 (2020).

[41] O. Schulz *et al.*, BAT.jl: A julia-based tool for bayesian inference, SN Comput. Sci. **2**, 210 (2021).